Seventh International Conference on
Computational Fluid Dynamics (ICCFD7),
Big Island, Hawaii, July 9-13, 2012

ICCFD7-2012-3604

DNS and ILES of transitional flows around a SD7003 using a high order Discontinuous Galerkin Method

C. Carton de Wiart[1,2] and K. Hillewaert[1,2]

[1] Cenaero

Rue des Frères Wright 29, B-6041 Gosselies, Belgium

[2] iMMC, Université catholique de Louvain

e-mails: *corentin.carton@cenaero.be, koen.hillewaert@cenaero.be*

Abstract: This paper is concerned with the ability of a high-order discontinuous Galerkin compressible flow solver to perform implicit large eddy simulation of transitional and turbulent flows. The approach is first validated on canonical test cases: the decay of homogeneous isotropic turbulence at very high Reynolds number and the channel flow at $Re_\tau = 395$. The method is first assessed with respect to referenced results: DNS or even theoretical behavior. The results are also compared with those obtained with SGS models implemented in spectral and finite volume codes. Finally, the method is applied on a more challenging test case: the flow past a SD7003 airfoil at $Re = 60k$ with an angle of attack $\alpha = 4°$. DNS as well as ILES have been performed and assessed with respect to the literature.

1   Introduction

In the near future the use of *Large Eddy Simulation (LES)* or even *Direct Numerical Simulation (DNS)* will become ever more widespread, e.g. for the prediction of flow instabilities and noise generation, or even simply the global performance of flow machinery. However, the use of these approaches requires highly resolved computations. Therefore, the discretisation method should feature a high order of convergence, as well as excellent parallel scaling to tackle the huge resolution requirements. An additional difficulty stems from the geometrical complexity of industrial geometries. Recently *finite element (FEM)*-like high-order methods such as *discontinuous Galerkin (DGM)* [1, 2], *spectral difference (SDM)* [3, 4] and *spectral element (SEM)* [5, 6] methods have been applied to such computations. The main motivation is that these methods bridge the gap between the high accuracy - deemed indispensable for adequate resolution of the turbulent structures - of academic solvers and the geometric flexibility of industrial solvers. In addition to very interesting dispersion and dissipation properties, DGM furthermore provides computational efficiency and a simple way of checking grid resolution without requiring additional computations. These advantages potentially make DGM a powerful tool for high fidelity simulation of transitional and turbulent flows.

An implicit time-integration DGM compressible flow solver has been assessed in a previous study for different orders of interpolation, with respect to a high-order finite difference (FDM) and a spectral code on DNS computations of the Taylor-Green vortex at $Re = 1600$ [7]. Although dissipative, DGM shows better accuracy for the same number of degrees of freedom as central (and hence dissipation-free) FDM of the same order of accuracy, probably due to better dispersion properties. The method has been further evaluated on more complex geometries such as the transitional flow around low Reynolds airfoils (Eppler E387 and SD7003, $Re = 60k$ with low angle of attack) or the flow past a low pressure turbine cascade at a realistic isentropic Reynolds number $Re_{is} = 85000$ [8].

The results of those validation showed that, for slightly under-resolved computations, the small features of the flow (i.e. the high wavenumbers) were dissipated by the discretisation scheme. Indeed, DGM only dissipates the scales that the model is not able to capture correctly, thus acting like a subgrid scale model. This property makes DGM an excellent candidate for implicit large eddy simulation (ILES).

The present study focuses on the validation of ILES of transitional flows using DGM. In the first part, the validation of ILES with DGM is performed on canonical test cases. The Homogeneous Isotropic Turbulence (HIT) at very high Reynolds number and the channel flow at $Re_\tau = 395$ [9] are considered. In the second part, the DNS and the ILES of the transitional flow past an airfoil are compared. The flow around a SD7003 airfoil at a Reynolds number equal to $60k$ with an angle of attack of $\alpha = 4°$ is considered. At this Reynolds number, the flow typically features a laminar separation, followed by transition in the resulting shear layer and a reattachment zone (figure 13). This benchmark has been already studied in several publications [10, 11, 12].
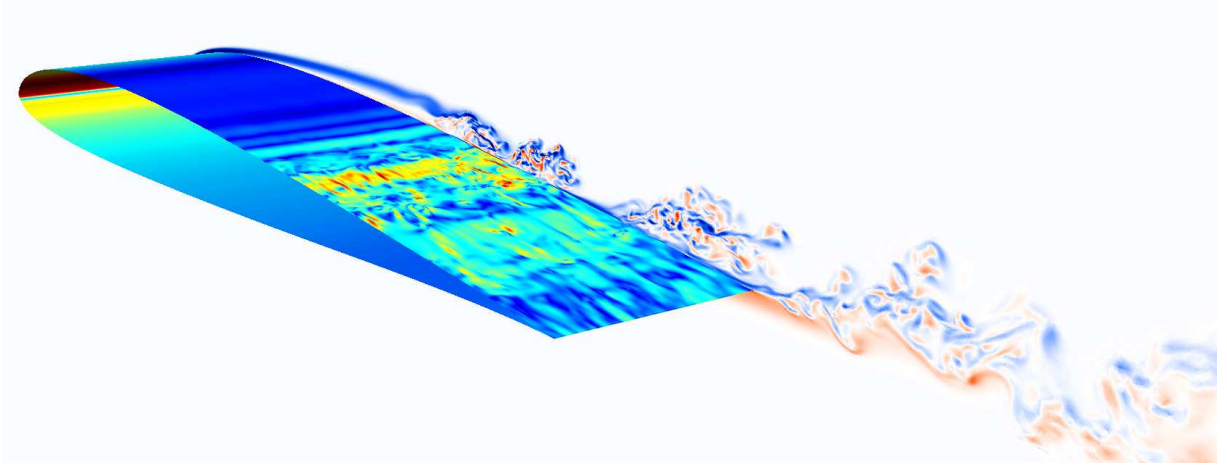

Figure 1: Instantaneous vorticity field on the periodic plane and skin friction on the surface of the airfoil.

The test case has also been selected for the first International Workshop on High-Order CFD Methods (Nashville, Tennessee, 2012).

2 Numerical methods

2.1 The discontinuous Galerkin / Symmetric Interior Penalty method

For compacity reasons, the compressible Navier-Stokes equations are written as a set of generic convection-diffusion equations for the state vector $\tilde{u}$ defined on domain Ω:

$$\frac{\partial \tilde{u}_m}{\partial t} + \frac{\partial}{\partial x^k}\left(\mathbf{f}_m^k(\tilde{u}) + \mathbf{d}_m^k(\tilde{u}, \nabla\tilde{u})\right) = 0 \ , \ \forall m \tag{1}$$

whereby appropriate Dirichlet and Neumann boundary conditions are defined on the boundary $\partial\Omega$. m is the index running on the different variables in the state vector. For the description of the discretisation of the viscous terms, we furthermore rely on a first order expansion of the diffusive fluxes:

$$\mathbf{d}_m^k \approx \mathcal{D}_{mn}^{kl}(\tilde{u})\frac{\partial \tilde{u}_n}{\partial x^l} \ .$$

2.1.1 Spatial discretisation

The discontinuous Galerkin method [13, 14] is a Galerkin finite element method based on an interpolation space Φ, composed of functions ϕ that are polynomials of order p on each of the elements e in the mesh E, but not required to be continuous across any of the interfaces f between elements. Such an interpolant is illustrated in figure 2.

The DGM then approximates component m of the solution state vector $\tilde{u}$ by u as

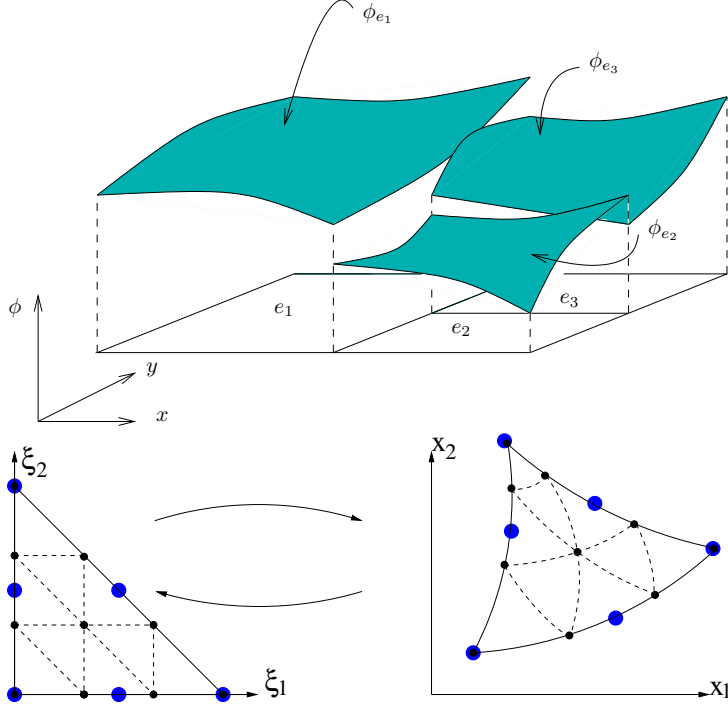$$u_m = \sum_i \mathbf{u}_{im}\phi_i \ , \ \phi_i \in \Phi \ .$$

Figure 2: The DGM interpolation space

As for any Galerkin method, the expansion weights $\mathbf{u}_{im}$ are found by requiring that the residual of the model equations, evaluated with u, is orthogonal to any function ϕ_i of the interpolation space Φ. This principle is further complemented with consistent and penalty terms on the element interfaces, using the Roe upwind flux for the convective terms whilst the diffusive terms are discretised according to the *Symmetric Interior Penalty (SIP)* method [14]:

$$
\forall \phi_i \in \Phi \;,\; \forall m : B(u, \phi)_m = \sum_e \int_e \phi_i \frac{\partial u_m}{\partial t} dV - \sum_e \int_e \frac{\partial \phi_i}{\partial x^k} (\mathbf{f}_m^k + \mathbf{d}_m^k) \; dV
$$

$$
+ \underbrace{\sum_f \int_f [[\phi_i]]^k \mathbf{n}^k \; \mathcal{H}_m \left(u^-, u^+, \mathbf{n} \right) dS}_{CI} + \underbrace{\sum_f \int_f [[\phi_i]]^k \{\{\mathcal{D}_{mn}^{kl} \; \frac{\partial u_n}{\partial x^l}\}\} dS}_{DI}
$$

$$
+ \underbrace{\sum_f \int_f [[u_n]]^k \{\{\mathcal{D}_{nm}^{kl} \cdot \frac{\partial \phi_i}{\partial x^l}\}\} dS}_{DS} + \underbrace{\sum_f \sigma \int_f [[u_m]]^k [[\phi_i]]^k dS}_{DP} = 0
$$

(2)

Using $+$ and $-$ to indicate lower and upper values with respect to the face normal $\mathbf{n}$, we define $\mathbf{n}^- = \mathbf{n}$ and $\mathbf{n}^+ = -\mathbf{n}$. The interface average $\{\{.\}\}$ and jump $[[.]]$ operators are then defined as

$$
\{\{a\}\} = \frac{a^+ + a^-}{2} \;,\; [[a]] = a^- \mathbf{n}^- + a^+ \mathbf{n}^+ \;.
$$

(3)

For the convective terms, the Riemann solver $\mathcal{H}$ assures the correct flux of characteristics sent to and received from neighbouring cells, thus assuring correctly posed elementwise problems and global energy stability. For the diffusive term the method generalises a boundary penalty method to enforce weak coupling at the interfaces. The penalty parameter σ must be chosen to be large enough to guarantee stability. Sharp

bounds for the value of σ have been elaborated for simplices [15], and recently for hybrid meshes [16].

All Dirichlet boundary conditions, both for the convective and diffusive terms are imposed weakly by providing a fictitious exterior state for the convective interface flux terms **CI**, the consistent diffusive flux **DI**, the symmetrising term **DS** and the penalty term **DP**. Neumann boundary conditions for the diffusive terms are enforced by modifying the consistent **DI** and symmetrising term **DS** on the concerned faces.

2.1.2   Discussion

The most intuitive interpretation of the method is then to see it as a collection of single element finite element problems, coupled through weak boundary conditions.

The main advantages of the method consist on the one hand of a high order of accuracy on unstructured meshes, resulting in interesting dissipation and dispersion properties and data locality on the other. The dispersion and dissipation errors are illustrated on figure 3. Even second order DGM ($p = 1$) presents very low dispersion errors, compared to centered finite difference (FD) schemes. The dissipation of the scheme becomes progressively more focused on the higher wave numbers, as the order of interpolation increases. This dissipation property of DGM makes it an excellent candidate for ILES.
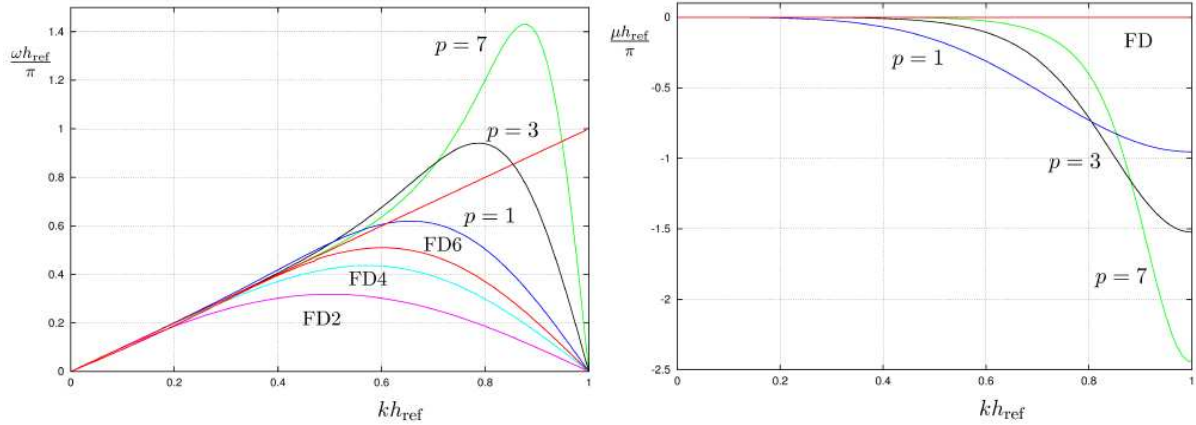

Figure 3: Dispersion (left) and dissipation (right) errors of DGM (p=1,3 and 7) compared with centered finite difference (order 2, 4 and 6) [17].

Finally, the data locality allows for a very efficient serial (see [18]) and parallel implementation, as illustrated by the weak parallel scaling of the implicit code as obtained on the Jülich BlueGene/P computer "Jugene", giving a 92% of efficient for $16k$ CPUs (figure 4). Therfore, the combination of those characteristics offers great potential for the use of DNS and LES computations of wall-bounded flows in complex geometry.

3   Validation of the method on canonical test cases

Before tackling complex geometries, the method will be validated on test cases for which detailed reference data are available. The HIT at very high Reynolds number is chosen to represent the behaviour of the method in the free-stream region of the flow. To assess the discretisation in the near-wall region, the channel flow at $Re_\tau = 395$ is considered.

3.1   HIT at very high Reynolds number

The flow is computed in a box, periodic in all three dimensions. A very high Reynolds number is considered with $\nu \to \infty$. The initial condition is generated with a pseudo-spectral code. After a given transient phase,
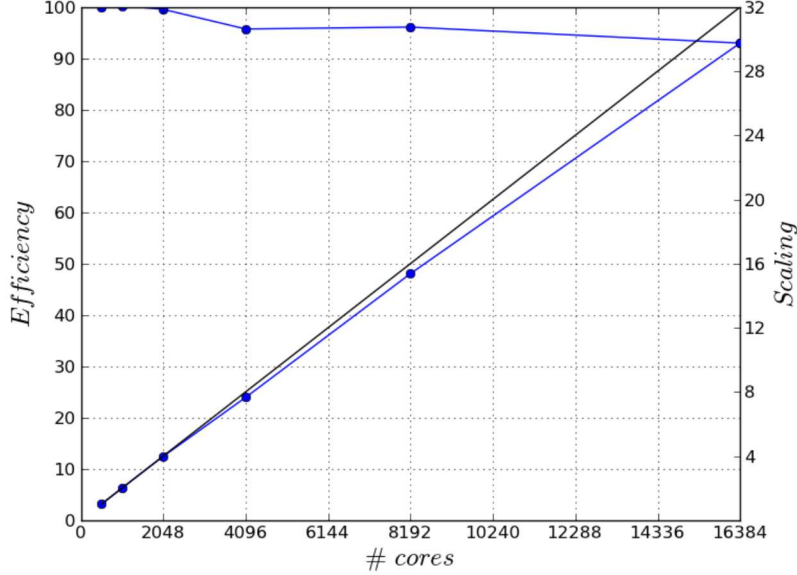
Figure 4: Weak scaling on Jugene.

due to the sudden absence of viscosity, the kinetic energy evolves following a power law

$$\frac{E(t)}{E_0} = \left(\frac{t}{t_0}\right)^{-\alpha}. \tag{4}$$

According to literature, the value of the decay exponent should be around $\alpha = 1.30 \pm 0.10$. In the spectral domain, the energy spectra should give a semi-infinite range, with a true $k^{-5/3}$ behavior according to Kolmogorov theory. The ILES approach has been used on a 64^3 and a 128^3 dof grid (i.e. 16^3 and 32^3 elements with $p = 4$). Figure 5 displays the temporal evolution of the energy. The results are coherent with literature: in the statistically developed regime, the kinetic energy decreases following an exponential law, around $\alpha = -1.3$. The energy spectrum presented in figure 6 is then computed by averaging the spectra in this regime. Only the 32^3 grid is presented as the spectral range of 16^3 is too short to obtain a true $k^{-5/3}$ behavior. The results are compared with those obtained by Cocle *et al.* [19] with a pseudo-spectral code on a 128^3 grid using different subgrid scale models: regularized variational multiscale (RVMs), hyperviscosity and Smagorinsky. It can be seen that the behavior of the ILES/DGM is very similar to the RVMs of the spectral code. The result is even a bit better for the larger wavenumber. Compared to Smagorinsky, which is the more commonly used SGS model, the results of DGM are much better, with a larger inertial range. It is important to notice that this result for ILES/DGM is obtained without constant tuning, as opposed to the SGS models.

3.2   LES of a turbulent channel flow

The turbulent channel flow test case at $Re_\tau = 395$ and low mach number $M = 0.1$ is chosen to assess the behavior of the method on wall-bounded flows. Furthermore, a large number of references are available in the literature [20, 21]). It consists in the simulation of the turbulent flow between two no-slip walls separated by a distance $2\,h$. The domain is periodic in the x and z direction and the size of the domain is $2\pi \times 2h \times \pi$. Usually, the velocity reference for this problem is the friction velocity u_τ which is linked to the average wall shear stress τ_w in the following way: $u_\tau^2 = \frac{\tau_w}{\rho}$. The flow is forced by a pressure gradient which is computed from the targeted Re_τ: $\frac{\partial p_f}{\partial x} = -\rho\frac{u_\tau^2}{h}$. The results of a fourth order accurate ($p = 3$) ILES/DGM are compared with DNS results of Moser and LES computations performed with a FVM solver by Georges *et al.* [22]. The

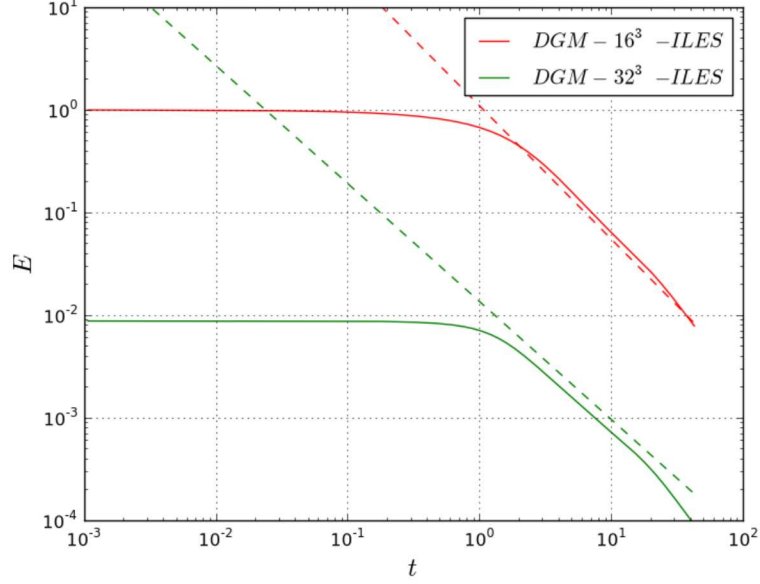Figure 5: Evolution of the kinetic energy for the HIT at very high Reynolds number. ILES/DGM results for two grids: 16^3 and 32^3.
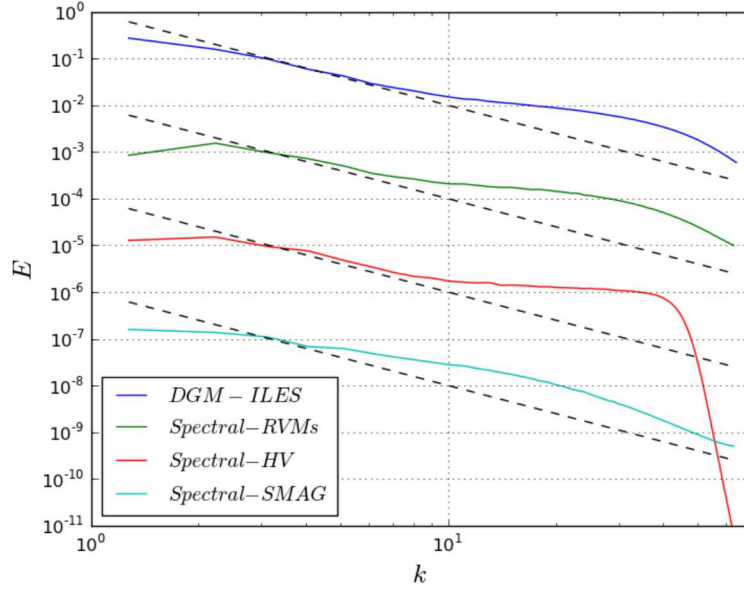

Figure 6: Energy spectra for decaying HIT. Results of ILES/DGM (blue) compared with those of a pseudo-spectral code with RVMs, hyperviscosity and Smagorinsky SGS model.

turbulence model used in this last computation is the filtered version of the WALE model as proposed by Bricteux *et al.* [21]. The number of dof for the LES computations are the same ($48 \times 48 \times 64$). The wall normal stretching used in both computations is slightly different. Nevertheless, studies with the FVM solver have shown that results are not significantly impacted by the mesh distribution if one consider wall resolved

LES. Third order polynomials are used for the DGM computation leading to fourth order accuracy in space. The temporal integration is performed with the second order implicit Three Points Backward Difference (3BDF) scheme. The time step is chosen as $\Delta t^+ = 0.002$, with $t^+ = \frac{t\,h}{u_\tau}$. $40t^+$ are necessary to obtain a statistically developed flow and $40t^+$ to converge statistics. Figure 7 displays the space and time averaged velocity profile in wall coordinates: $u^+ = u/u_\tau$ as a function of $y^+ = y\,u_\tau/\nu$. The results obtained by
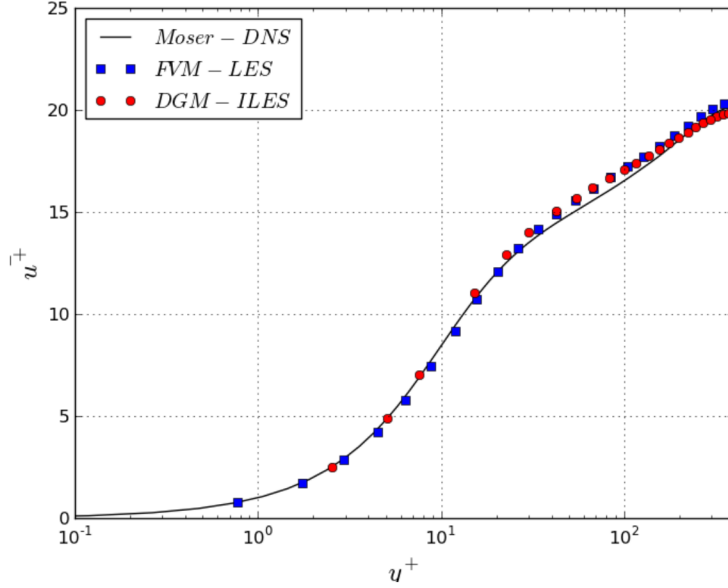

Figure 7: Mean velocity profile for the channel flow at $Re_\tau = 395$.

both computations are close, except near the center of the channel where the FVM seems to over-predict the velocity. The differences between the computations are clearer when comparing the computed velocity variances ($\overline{u'u'}$, $\overline{v'v'}$ and $\overline{w'w'}$), as presented in figure 8. The DGM simulation seems to be more accurate, even if some oscillations are present around $y^+ = 40$. The results are even better when looking at the covariance Reynolds shear stress $-\overline{u'v'}$. Here, the DGM result is almost perfectly superimposed with that
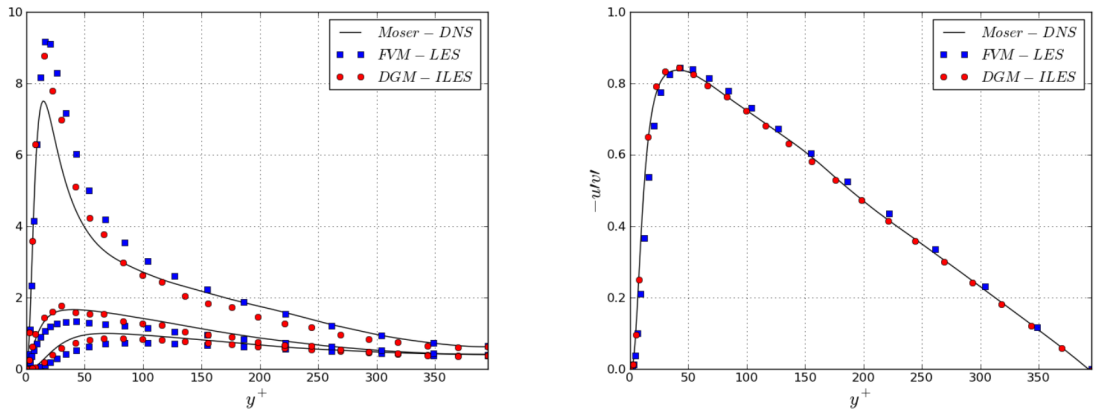

Figure 8: Velocity fluctuations (left, $\overline{u'u'}$ (top), $\overline{w'w'}$ (mid) and $\overline{v'v'}$ (bottom)) and Turbulent mean shear stress profile (right, $-\overline{u'v'}$) of the simulation of the channel flow at $Re_\tau = 395$.

7

of the reference while the curve obtained with FVM is slightly shifted to the right. Here again, as in the HIT case, it is important to note that the coefficient of the SGS model used for the FVM computations needed to be calibrated to obtain the best fit with the reference. Obviously, an ILES approach does not need such a calibration, and the DGM method finds itself the right amount of dissipation. This property is very interesting for industrial applications, where the use of dynamic procedures for the computation of the model coefficient is very difficult to use and does not always provide accurate results.

4 DNS and ILES of the flow past the SD7003 airfoil

In this section, DNS and ILES of the flow past a SD7003 at $Re = 60000$ and $M = 0.1$ are performed using a fourth order accurate DGM ($p = 3$). A non swept, constant chord wing is considered with an aspect ratio equal to 0.2 (following Galbraith [12]) and an angle of attack of 4°. The motivation to perform a DNS was due to the lack of real reference solution in the literature. Only LES and ILES can be found and the results were not totally in agreement.

4.1 Numerical setup and mesh

For both computations, the temporal integration is performed using the 3BDF scheme. The time step is the same for both computations and is equal to $\Delta t = t_c/1000$ with $t_c = c/U_\infty$ the convective time. Periodic boundary conditions are imposed in the spanwise direction to simulate an infinite wing. Free-stream boundary conditions are weakly imposed on the other surfaces. Those are located at a distance equal to 100 chords away from the airfoil to avoid strong interactions with the latter. The grids are constructed by extruding an unstructured two-dimensional mesh resulting in a mesh composed of hexahedra and wedges. The mesh size of the extrusion is chosen to obtain a uniform mesh in the turbulent region. Two meshes have been considered in this study: one designed for DNS and one for LES. For both grids, the grid specifications have been determined during a number of preliminary two dimensional runs such as to ensure sufficient resolution near critical regions of the laminar region (laminar boundary layer separation point). Refinement boxes are placed in the turbulent region and in the wake of the flow (see figure 10). The mesh size in these refinement boxes is four times coarser for the LES than for the DNS. The boundary layer mesh has a first layer size equal to $\Delta y_0/c = 3.33 \ 10^{-4}$ and a growth rate of $r = 1.2$. Figure 9 and 10 show the resulting DNS and LES meshes.
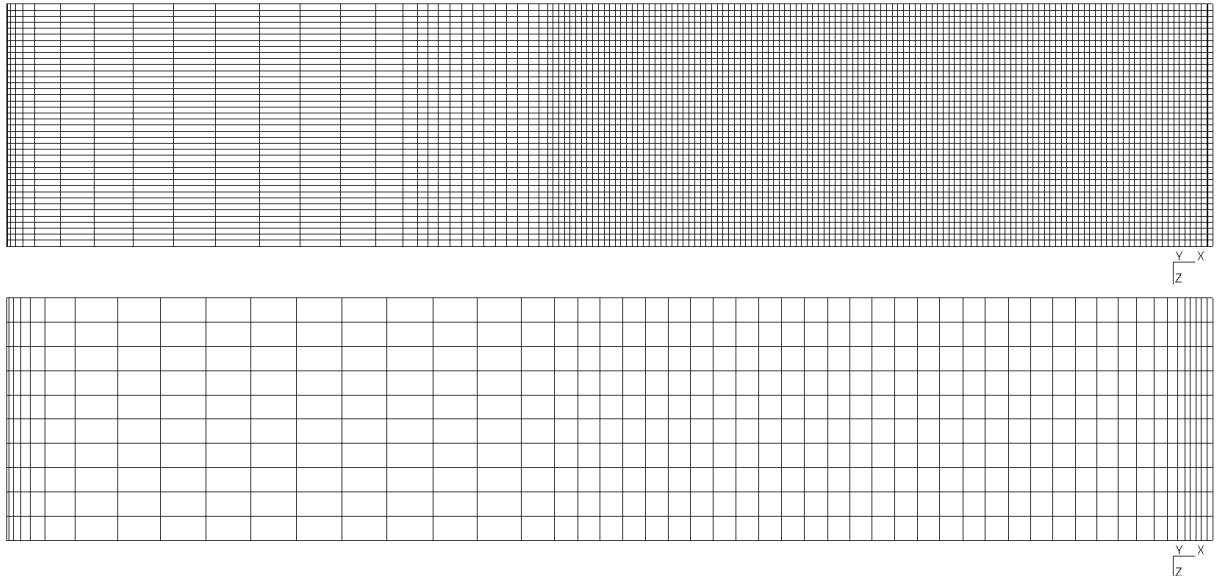

Figure 9: Comparison between DNS (up) and LES (down) mesh at the suction side of the airfoil.
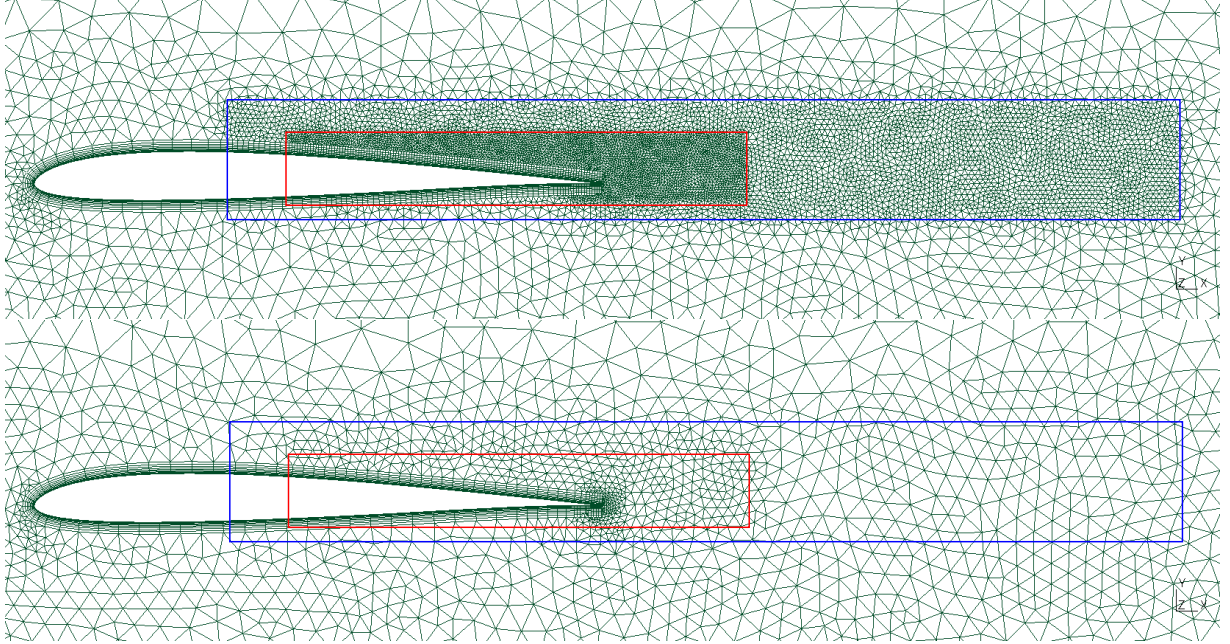
Figure 10: Comparison between DNS (up) and LES (down) mesh at the periodic plane. Refinement box 1 (red) and 2 (blue) are also shown.

Table 4.1 summarizes the mesh size in different regions of the flow, the mesh size at the wall in the turbulent region (at $x/c = 0.8$) and the total size of the mesh. As the computation is fourth order accurate (with $p = 3$), the mesh sizes correspond to the distance between two high-order nodes, i.e. the size of an element divided by p.

	DNS	LES
$\Delta y_0/c$ (wall-normal)	$3.33\ 10^{-4}$	$3.33\ 10^{-4}$
$\Delta x/c$ (box 1)	$1.67\ 10^{-3}$	$6.67\ 10^{-3}$
$\Delta x/c$ (box 2)	$3.33\ 10^{-3}$	$1.33\ 10^{-2}$
$\Delta z/c$ (spanwise)	$1.67\ 10^{-3}$	$6.67\ 10^{-3}$
y^+ at $x/c = 0.8$	1.2	1.2
$x^+ = z^+$ at $x/c = 0.8$	6	24
Number of hexahedra (/1000)	84.7	8.7
Number of wedges (/1000)	646.1	47.9
Total number of dof per variable (at continuity) [k]	10934.3	874.5

Table 1: Mesh characteristics for DNS and LES.

4.2 Preliminary unsteady results

Figure 11 shows the time evolution of the lift and the drag coefficients for both computations. The ILES has been running for $45t_c$ and the DNS for $40t_c$. Even if the lift coefficients have converged to a value around $C_L = 0.6$, the drag coefficients still globally increase. This means that the flows have not completely reached a statistical developed state. The time needed to obtain a statistically converged solution is longer than what has been reported in literature (Uranga et al. [11]) and this may be due to the large size of the computational domain. Nevertheless, both computations are converging to the same values, in agreement with the literature. Due to a lack of time, a preliminary analysis is done in this section on the last timesteps
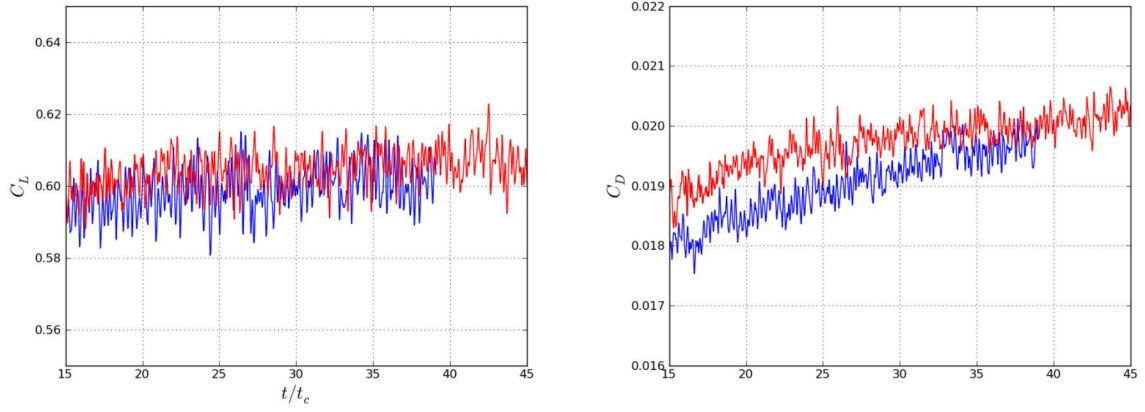
9

Figure 11: Temporal evolution of the lift (left) and drag (right) coefficients for DNS (blue) and ILES (red).

obtained. Fully converged results will be presented at the conference.

Instantaneous velocity fields are presented for both computations in figure 12. The flow fields are globally in agreement: the separation point, the transition position and the turbulent region are located at the same position in both computations. As expected, the small turbulent structures that can be seen on the DNS are filtered by the mesh in the LES. Nevertheless, the larger energetic scales seem to be well captured; the flow is globally continuous in all regions of the flow.
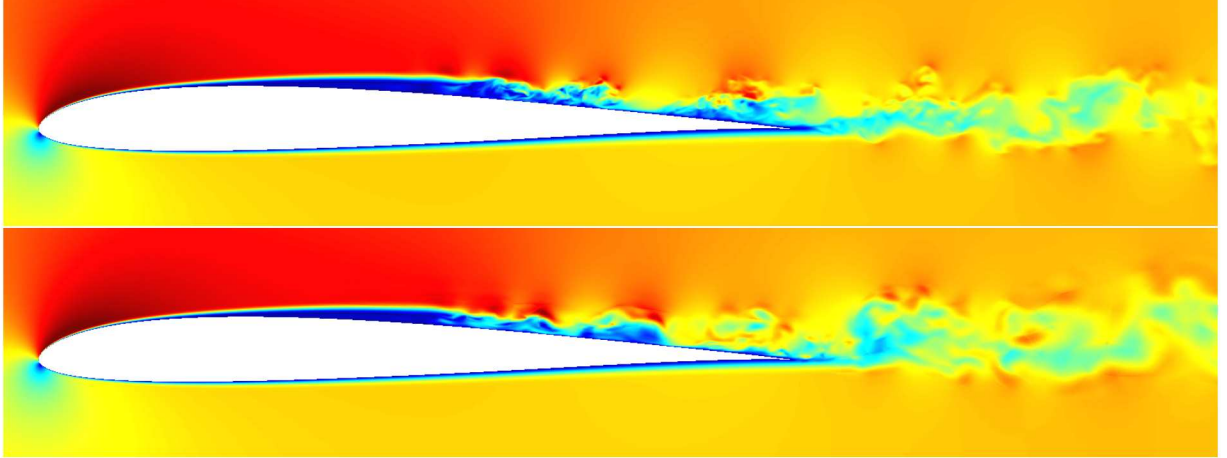

Figure 12: Snapshot of the velocity norm. DNS (top) and LES (bottom).

Therefore, strong discontinuities can be seen on the vorticity field for the LES at the contrary to the DNS where the field is globally continuous, assessing the adequate resolution of the computation (figure 13). Small turbulent structures are generated near the bursting of the shearlayer. Even if the scales are larger in the LES, the magnitude of those vortices are similar to the DNS.

The same remark can be made from the friction coefficient at the suction side of the airfoil (figure 14). The structure are larger in the LES and some discontinuities can be seen in the field. Nevertheless, the position, the pattern and the magnitude of the large scales are in good agreement.
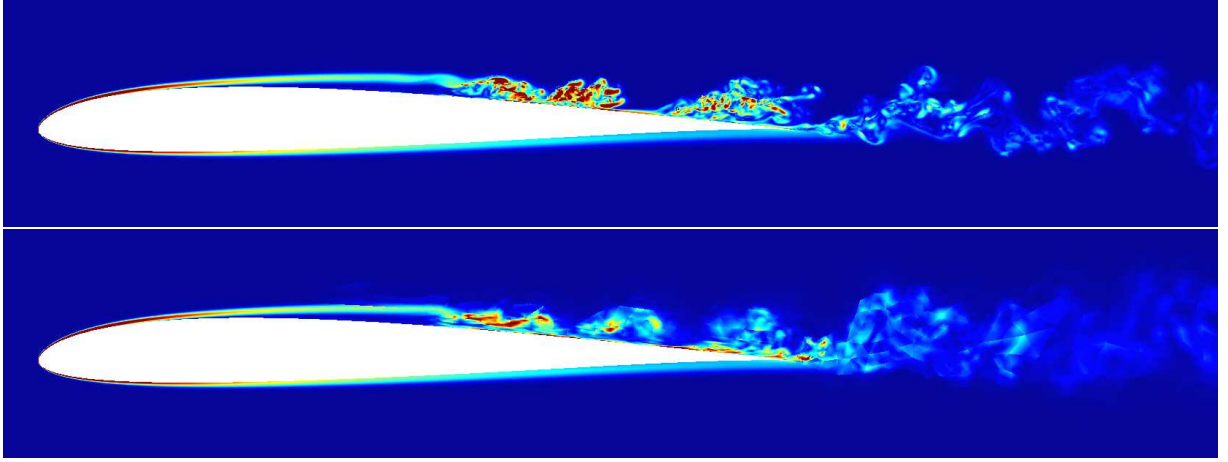
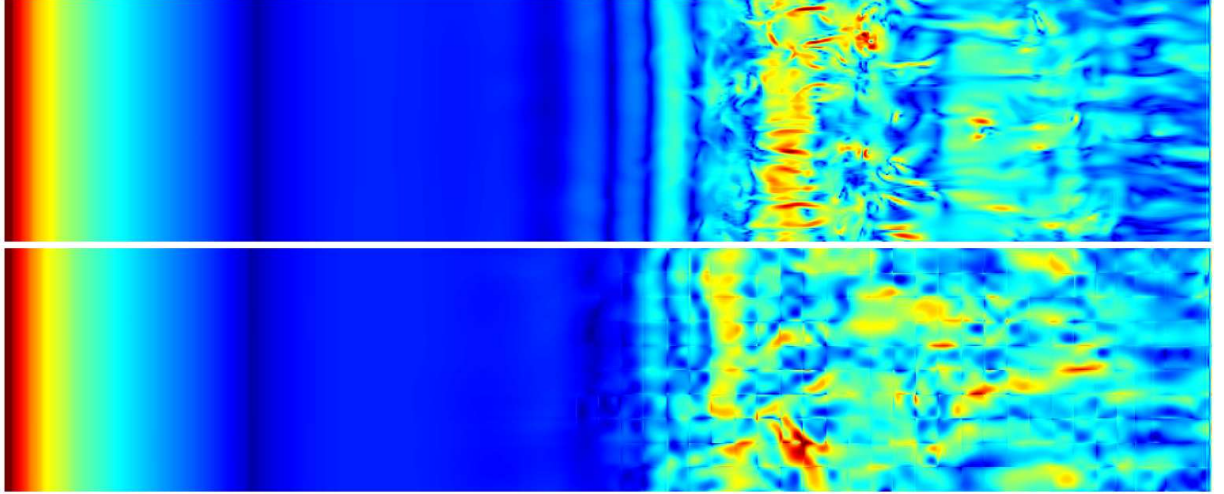Figure 13: Snapshot of the vorticity norm. DNS (top) and LES (bottom).

Figure 14: Snapshot of the friction at the wall. DNS (top) and LES (bottom).

4.3 Averaged flow fields

All the quantities of interest are averaged during the last $5t_c$. Figure 15 shows the averaged value of the pressure and the friction coefficients at the surface of the airfoil. The same behavior is obtained for both coefficients. Only small differences can be seen on the pressure coefficient at the transition region and a slight overprediction of the friction coefficient for the ILES in the turbulent region.

Figure 16 compares the pressure and friction coefficients of the DNS/DGM with those of LES found in the literature [11]. Results are globally in good agreement, the LES curves are located around the DNS/DGM. Nevertheless, the differences between the computations are more pronounced than what can be observed on figure 15.

Table 4.3 compares the results of the two DGM computations (DNS and ILES) with those obtained by the ILES of Galbraith [12] and Uranga [11], on a $4.8M$ grid and a $1.8M$ grid respectively. The computational times are also presented for DGM. Results are globally in agreement, especially with Uranga et al.[11]. Only a discrepancy can be found in the mean drag coefficient, but as shown on figure 11, the drag of DGM computations seems to converge to the same value as Uranga. ILES/DGM is able to globally reproduce the major quantities of the flow at a cost 25 times lower than the DNS. Nevertheless, those results have to be validated and confirmed on more converged results.
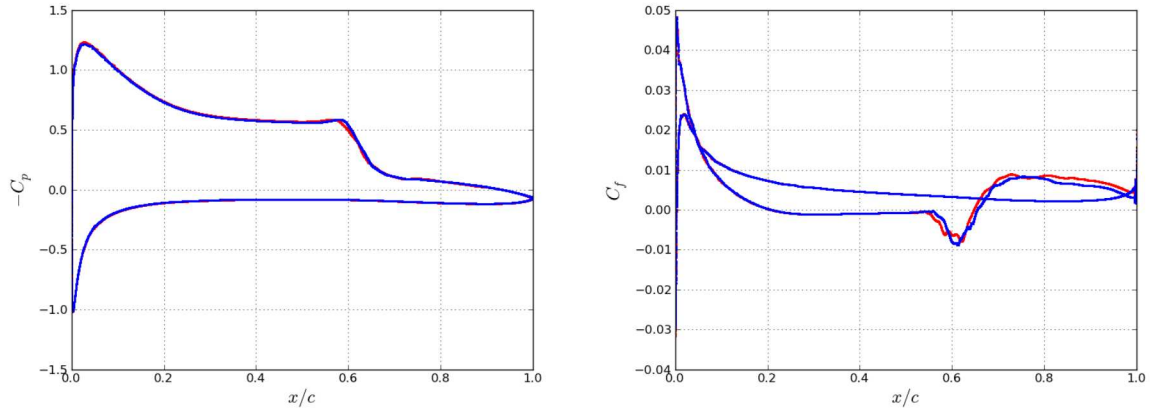
11

Figure 15: Mean pressure (left) and friction (right) coefficients for DNS (blue) and ILES (red).
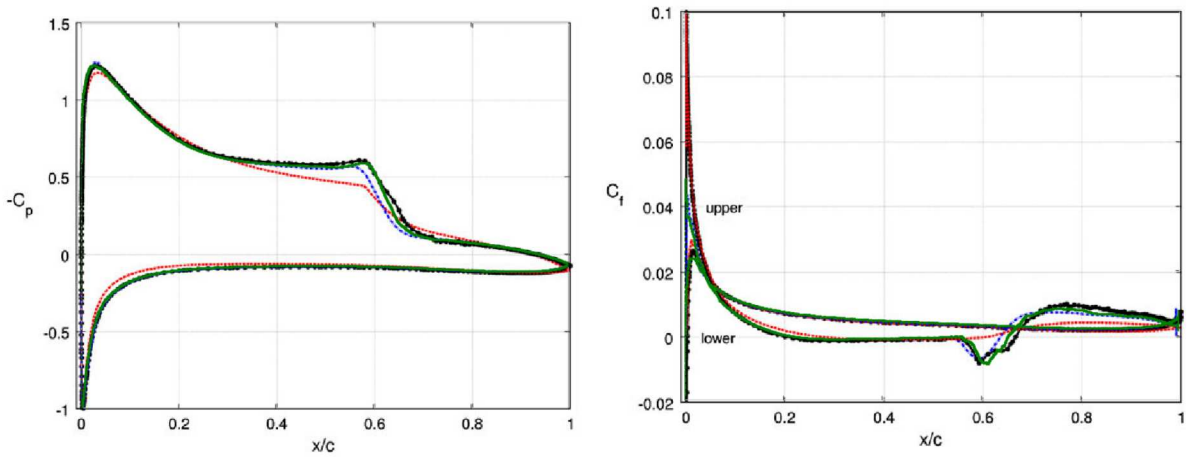

Figure 16: Mean pressure (left) and friction (right) coefficients for DNS (green), Uranga (black), Galbraith (blue) and XFOIL (red). Source: Uranga et al. [11].

	DNS/DGM	ILES/DGM	Uranga [11]	Visbal [12]
$\overline{C_L}$	0.196	0.201	0.22	-
$\overline{C_D}$	0.602	0.607	0.603	-
Separation	0.209	0.207	0.21	0.23
Reattachment	0.654	0.647	0.65	0.67
Cost to compute one t_c [CPUh]	11001	415	-	-

Table 2: Averaged results. Comparison between DNS, ILES and literature.

5 Conclusion

The ability of DGM to perform efficient ILES has been assessed on canonical test cases and applied to a more advanced benchmark. The canonical test cases have been chosen to represent free turbulence (HIT at infinite Reynolds) and wall-bounded turbulence (channel flow at $Re_\tau = 395$). For the HIT at infinite Reynolds, the results are in agreement with theory. The results are also very close to those obtained with a spectral code using state-of-the-art SGS models. For the channel flow, the results are in agreement with

the DNS reference of Moser et al. [20]. The results are even slightly closer to the DNS than those obtained with a second-order finite volume method using RVMs. Finally, the method has been applied to a more challenging test case: the transitional flow around a SD7003 airfoil at $Re = 60k$ with an angle of attack of $4°$. As no references were found in the literature, a DNS has been also performed. Both meshes have been designed to fit with DNS and LES constraints. To assess the quality of the DNS, the global continuity of the flow field (velocity, vorticity and skin friction) have been verified with success. The ILES is very close to the DNS for every quantities, despite the coarse mesh. Both computations are also globally in agreement with the literature [11, 12]. Unfortunately, the computations were not fully statistically converged but the results are very encouraging. Statistically converged results will be presented at the conference.

References

[1] F. van der Bos and B.J. Geurts. Computational error-analysis of a discontinuous Galerkin discretization applied to large-eddy simulation of homogeneous turbulence. *Computer Methods in Applied Mechanics and Engineering.*, 199(13-16):903–915, 2010.

[2] L. L. Wei and A. Pollard. Direct numerical simulation of compressible turbulent channel flows using the discontinuous Galerkin method. *Computers and Fluids*, 47:85–100, 2011.

[3] Y. Zhou and Z.J. Wang. Effects of Surface Roughness on Laminar Separation Bubble over a Wing at a Low-Reynolds Number. In *Proceedings of the 49th AIAA Aerospace Sciences Meeting*, number AIAA 2011-736, Orlando, Florida, January 2011.

[4] C. Liang, S. Premasuthan, and A. Jameson. Large Eddy Simulation of Compressible Turbulent Channel Flow with Spectral Difference method. In *47th AIAA Aerospace Sciences Meeting*, number AIAA 2009-402, Orlando, Florida, January 2009.

[5] J. Ohlson. *Spectral-element simulations of separated turbulent internal flows.* PhD thesis, Kungliga Tekniska Hogskolan Stockholm, 2009.

[6] C.E. Wasberg, T. Gjesdal, B.A Pettersson Reif, and O. Andreassen. Variational multiscale turbulence modelling in a high order spectral element method. *Journal of Computational Physics*, 228:7333–7356, 2009.

[7] C. Carton de Wiart, K. Hillewaert, M. Duponcheel, G Winckelmans, and P. Geuzaine. Direct Numerical Simulation of the Taylor-Green vortex using a high-order Discontinuous Galerkin Methods. *In preparation.*

[8] C. Carton de Wiart, K. Hillewaert, and P. Geuzaine. DNS of a low pressure turbine blade computed with the Discontinuous Galerkin Method. In *Proceedings of ASME Turbo Expo 2012*, Copenhagen, Danemark, June 2012.

[9] C. Carton de Wiart, K. Hillewaert, P. Geuzaine, R. Luccioni, L. Bricteux, G. Coussement, and G. Winckelmans. Assessment of LES modeling within a high order Discontinuous Galerkin solver. In *Proceedings of ETMM9*, Thessaloniki, Greece, June 2012.

[10] Y. Zhou and Z.J. Wang. Implicit Large Eddy Simulation of Transitional Flow over a SD7003 Wing Using High-order Spectral Difference Method. In *Proceedings of the 40th AIAA Fluid Dynamics Conference and Exhibit*, number AIAA 2010-4442, Chicago, Illinois, June 2010.

[11] A. Uranga, P.-O. Persson, M. Drela, and J. Peraire. Implicit Large Eddy Simulation of Transitional Flows over Airfoils and Wings. In *Proceedings of the 19th AIAA Computational Fluid Dynamics*, number AIAA 2009-4131, San Antonio, Texas, June 2009.

[12] M. Galbraith and M. Visbal. Implicit large-eddy simulation of low reynolds number ïňĆow past the sd7003 airfoil. In *Forty-sixth AIAA Aerospace Sciences Meeting and Exhibit*, Reno, NV, January 2008.

[13] B. Cockburn, G.E. Karniadakis, and C.-W. Shu. The development of discontinuous Galerkin methods. In B. Cockburn, G. E. Karniadakis, and C.-W. Shu, editors, *Discontinuous Galerkin Methods*, pages 3–50. Springer, 2000.

[14] D.N. Arnold, F. Brezzi, B. Cockburn, and L.D. Marini. Unified Analysis of Discontinuous Galerkin Methods for Elliptic Problems. *SIAM J. Num. Anal*, 39:1749–1779, 2002.

[15] K. Shahbazi. An explicit expression for the penalty parameter of the interior penalty method (Short note). *Journal of Computational Physics*, 205:401–407, 2005.

[16] K. Hillewaert, J.-F. Remacle, and M. Drosson. Sharp constants in the hp-finite element trace inverse

inequality for standard functional spaces on all element types in hybrid meshes. *Submitted to the SIAM Journal of Numerical Analysis*, 2011.

[17] Paul-Emile Bernard. *Discontinuous Galerkin methods for geophysical flow modeling*. PhD thesis, Université Catholique de Louvain, 2008.

[18] K. Hillewaert. *ADIGMA - A European Initiative on the Development of Adaptive Higher-Order Variational Methods for Aerospace Applications - Results of a collaborative research project funded by the European Union, 2006-2009*, volume 113 of *Notes on Numerical Fluid Mechanics and Multidisciplinary Design*, chapter Chapter 2: Exploiting data locality in the DGM discretisation for optimal efficiency, pages 11–24. Springer, 2010.

[19] R. Cocle, L. Bricteux, and G. Winckelmans. Scale dependence and asymptotic very high reynolds number spectral behavior of multiscale subgrid models. *Physics of Fluids*, 21(8), 2009.

[20] R. D. Moser, J. Kim, and N. N. Mansour. Direct numerical simulation of turbulent channel flow up to retau=590. *Physics of Fluids*, 11(943), 1999.

[21] L. Bricteux, M. Duponcheel, and G. Winckelmans. A multiscale subgrid model for both free vortex flows and wall-bounded flows. *Physics of Fluids*, 21(105102), 2009.

[22] L. Georges and P. Geuzaine. On kinetic energy conserving schemes for large eddy simulations on unstructured meshes. In *Proceedings of the Third International Conference on Advanced Computational Methods in Engineering*, Ghent, Belgium, June 2005.